Materials & Design 185 (2020) 108243

Contents lists available at ScienceDirect

Materials & Design

journal homepage: www.elsevier.com/locate/matdes

Manufacturing bioinspired flexible materials using ultrasound directed self-assembly and 3D printing

Paul Wadsworth, Isaac Nelson, Debora Lyn Porter, Bart Raeymaekers, Steven E. Naleway *

University of Utah, Department of Mechanical Engineering, 1495 E 100 S (1550 MEK), Salt Lake City, UT, 84112, USA

HIGHLIGHTS

- Direct-write 3D printing and ultrasound directed self-assembly were combined to form user-defined micro-structured materials.
- Discontinuous lines of aligned microfibers were formed via the applied ultrasound field with varying operating frequencies.
- The number and spacing of parallel lines of aligned microfibers were shown to differ between different operating frequencies.
- Electrical conductivity was observed in the aligned microfibers, suggesting that the electrical properties could be tailored.
- The ultrasound direct-write process created flexible single layer samples with integrated lines of aligned microfibers.

GRAPHICAL ABSTRACT

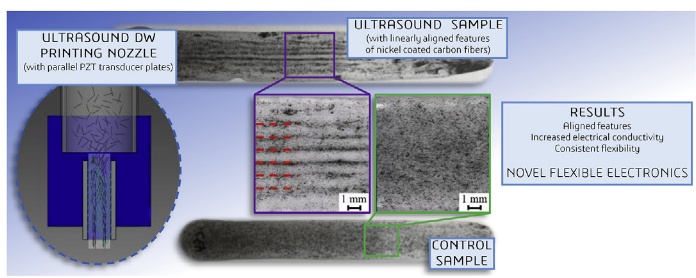

ARTICLE INFO

Article history:
Received 19 August 2019
Received in revised form
25 September 2019
Accepted 26 September 2019
Available online 10 October 2019

Keywords:
3D printing
Ultrasound directed self-assembly
Bioinspired materials

ABSTRACT

Biological materials that are composed of hierarchical microstructures embedded in a matrix material can display enhanced mechanical or material properties compared to an unstructured mixture of the same constituent materials. In this work, ultrasound directed self-assembly was integrated with 3D printing (direct-write (DW)) in a new manufacturing process called “ultrasound DW”, to enable the fabrication of engineered materials with properties mimicking those of natural materials. This process allows 3D printing feedstock that consists of a liquid photopolymer resin with dispersed microfibers, and enables fabricating materials with lines of aligned carbon microfibers. The effect of the ultrasound operating frequency and print speed on the alignment of the fibers, distance between adjacent lines of aligned fibers, as well as the resulting electrical conductivity and mechanical properties of the samples were evaluated. The results showed that the lines of aligned fibers in the material samples display statistically significant differences in terms of the distance between the adjacent lines of aligned fibers when looking at the factors of the ultrasound operating frequency and the print speed. The lines of aligned fibers form local percolated networks resulting in electrically conductive areas. The ultrasound

* Corresponding author.
E-mail address: steven.naleway@mech.utah.edu (S.E. Naleway).

https://doi.org/10.1016/j.matdes.2019.108243

DW process allows the fabrication of materials with integrated substructures that tune specific material properties.

1. Introduction

Biological materials that are composed of multiscale hierarchical microstructures embedded in a matrix material typically display different or even enhanced mechanical or material properties compared to an unstructured mixture of the same constituent materials [1,2]. For example, Bouligand-type structures of linearly aligned fibers within individual layers acting in tandem with a periodically skewed angle of orientation between each layer enhance the mechanical properties of various biological materials, such as the hammer-like composite structure of the dactyl club of marine stomatopods [3] and the natural dermal armor composed of mineralized collagen fibril structures in a species of fresh water fish called *arapaima gigas*, which are used as protection against piranhas [4]. Researchers have designed engineered materials with purposely integrated microstructures inspired by biological materials to mimic their mechanical and material properties, or even implement specific mechanical and material properties by tailoring the microstructure [5–8]. Specifically, several publications demonstrate the ability to control electrical properties of polymer-based engineered bioinspired materials, including carbon nanotube and graphene-based actuators that mimic muscle functions [9], bio-compatible polymers doped with conductive nanoparticles [10], and conductive composite graphene films inspired by the natural brick and mortar structure of nacre [11].

The ability to fabricate engineered materials with hierarchical microstructures that mimic biomaterials, and derive their function from aligned particles embedded within a polymer matrix, is of interest to a broad range of research fields and applications [12], including manufacturing of flexible biosensors and electrodes and the integration of electrical conductors in parts or assemblies. Fabricating hierarchical microstructures into engineered materials has previously been accomplished using a magnetic field in combination with stereolithography [13], traditional mold casting [14,15], and freeze casting [6,16–18]. Electric fields in combination with molding microwires from colloidal suspensions of metallic nanoparticles in water have also been used [19]. These fabrication methods enable manufacturing of homogeneous composite materials and some have been combined with 3D printing, including electric field 3D printing [20], shear force assisted 3D printing [21,22], and bioinspired 3D printing [23,24]. However, these fabrication techniques place strict requirements on material choice, possible material geometry, and dimensional scalability, often requiring ultra-high field strengths [25,26]. Thus, they may limit the potential properties and usefulness of the resulting engineered materials. In contrast, ultrasound directed self-assembly is based on the acoustic radiation force associated with a standing pressure wave, and has been used to orient and locate individual particles [27], separate or concentrate particles before deposition in a 3D printing application [28], self-assemble 2D [29] and 3D [30] patterns of particles in a liquid polymer, and fabricate single layer [31] and multilayer material structures [32] by combining ultrasound directed self-assembly with stereolithography 3D printing.

In this paper, we show that combining ultrasound directed self-assembly with direct-write (DW) 3D printing enables the fabrication of engineered materials with a hierarchical microstructure. The DW process, where a liquid feedstock is extruded through a syringe in user defined locations, allows for dimensional scalability, whereas ultrasound directed self-assembly enables control of the hierarchical microstructure. We will refer to this process as “ultrasound DW”, and demonstrate the fabrication of linear microstructures in combination with macroscale build-up of the material.

2. Materials and methods

2.1. Ultrasound DW setup

Fig. 1 shows the experimental setup used for this work. It comprises a Cartesian-style material extrusion type 3D printer (RepRapGuru, Myrtle Beach, SC, USA), where the print head assembly was replaced with a custom syringe print head designed and fabricated in our lab specifically to accept liquid photopolymer resin feedstock (UV Cure 60–7108 Non-Yellowing Adhesive and Potting Compound, Epoxies ETC., Cranston, RI, USA) instead of the traditional solid filament feedstock. The syringe plunger was actuated via a power screw assembly. Three different syringes were modified with permanently installed custom nozzles with

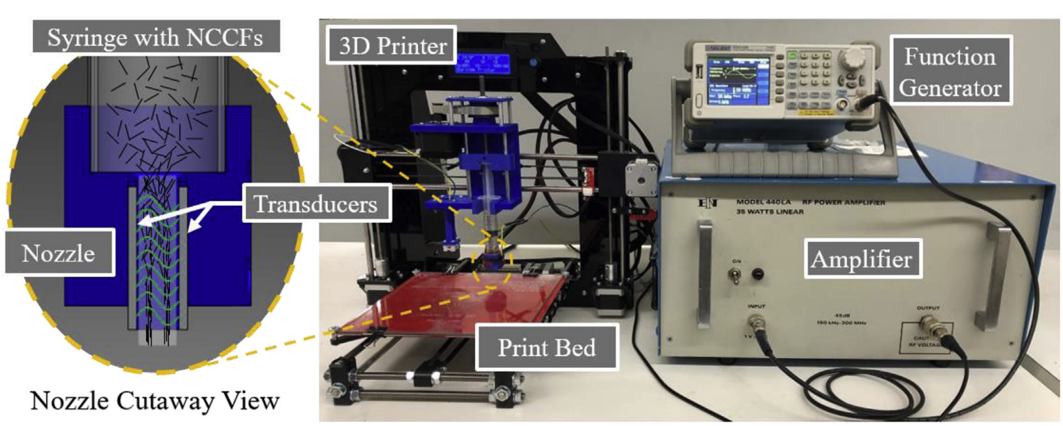

Fig. 1. Ultrasound DW setup. Fibers are aligned by the acoustic radiation force field generated by the transducers before being extruded from the nozzle (shown in blue) and deposited on the print bed.

integrated 20×15 mm piezoelectric plates made from a PZT-4 (Navy Type I) material (Steiner & Martins, Inc., Doral, FL, USA) as ultrasound transducers. These custom nozzles were driven by a function generator (Siglent Technologies, Solon, OH, USA) and 45 dB RF amplifier (ENI 440LA, Rochester, NY, USA), to perform ultrasound directed self-assembly of microscale nickel-coated carbon fibers (NCCFs) (100 μm length, 10 μm diameter, Conductive Composites, Heber City, UT, USA) dispersed in the photopolymer resin, into discontinuous line patterns. The center frequencies f_c of the piezoelectric plates were 1.0, 1.5, and 2.0 MHz, respectively, which were determined based on space considerations inside the print head, the sound propagation velocity of the photopolymer resin ($c = 1353$ m/s), and the number of resulting parallel lines of fibers in the photopolymer resin, $N = 2d/\lambda$, as previously demonstrated by Haslam et al. [33] and others [34–37]. Here $d = 5$ mm is the distance between the parallel piezoelectric plates, and λ is the wavelength of the standing pressure wave with $\lambda = c/f_c$. Fig. 1 shows that the entire height of the piezoelectric plate was exposed to the photopolymer resin exiting the syringe during the DW process, which created a $5 \times 5 \times 15$ mm^3 volume where the ultrasound directed self-assembly of the microfibers dispersed in the photopolymer resin took place, before extrusion through the nozzle and deposition onto the build platform.

2.2. Sample preparation

The liquid feedstock for the ultrasound DW process comprised 1 wt percent NCCFs and 99 wt percent photopolymer resin. NCCFs were chosen for this research to compare to previously reported results [32] and allow for a percolated network of electrically conductive fibers. The mixture of fibers and liquid matrix material was sonicated at 42 kHz for 3 min to disperse the NCCFs in the photopolymer resin, prior to transferring it into the syringe with the custom nozzle described in Section 2.1. Single-layer material samples were prepared by exposing the extruding feedstock to a standing ultrasound wave with frequency of either 0 Hz (no applied ultrasound as a control), 1.0 MHz, 1.5 MHz, or 2.0 MHz, using the nozzle with piezoelectric actuators of the corresponding center frequency, and printing a single-layer strip of $80 \times 10 \times 1$ mm on a Delrin® plastic substrate. In addition, to determine the impact of fiber loading on the mechanical properties, samples with 3 and 5 wt percent NCCFs were fabricated using the same procedures as samples with 1 wt percent NCCFs. Though possible, 3D printing of multi-layer samples was beyond the scope of this research. Each sample required approximately 1.2 mL of liquid feedstock. Control samples were fabricated without ultrasound exposure (0 Hz), and result in randomly oriented NCCFs. All samples were fabricated using three different print speeds, 2.15 mm/s, 4.25 mm/s, and 6.35 mm/s, the fastest of which created a volumetric feedstock print rate that is similar to standard 3D printing rates. After printing, each specimen was cured with a 3 Watt ultra-violet (UV) light source (365 nm wavelength) within the first 30 s to prevent movement of the aligned features of NCCFs due to the sustained flow of the uncured printed material on the build platform before exposure to a 36 Watt UV light source curing station. Note that, while not experimentally measured, the NCCFs displayed no visible movement during this 30 s time frame. Six samples were printed for each ultrasound frequency (including no applied frequency as a control) and print speed combination all at 1 wt percent NCCFs, i.e., 72 samples total.

2.3. Material characterization

Each sample was imaged using optical microscopy at 100× magnification, illuminated from both sides (Keyence VHX-5000, Itasca, IL, USA), covering the entire sample surface by sequentially imaging sections and stitching them together. Since the photopolymer cures optically transparent, the fibers were easily detected throughout each sample. In addition, to visualize NCCF alignment, samples were freeze fractured in liquid nitrogen and imaged using an SEM (FEI Quanta, Hillsboro, OR, USA). The distance between the parallel lines of aligned NCCFs was measured at 40 distinct points uniformly distributed along the length of the sample, using ImageJ image processing software (National Institutes of Health, Bethesda, MD, USA). Furthermore, the relative NCCF density along the width of each sample was qualified by computing the average pixel gray value of the 8-bit thresholded image for each horizontal line of pixels in the image. Each image was rotated (if necessary) to ensure the parallel lines of aligned NCCFs were parallel to the horizontal edges of the image and, therefore, each line of analyzed pixels. The average pixel gray value increases with increasing NCCF density. For each sample, the maximum and minimum average pixel gray value within the center section of the sample was recorded, avoiding measurements within 1.5 cm of the sample edges where edge-effects may have occurred. The spread was defined as the difference between the maximum and minimum average gray value, which quantitatively described the change in relative NCCF density across the width of the sample.

2.4. Electrical characterization

The electrical conductivity was quantified for two samples fabricated with each printing speed and ultrasound operating frequency combination, and for three control samples, i.e., a total of 21 samples. Note that electrical conductivity was only characterized in samples with 1 wt percent NCCFs Fig. 2(a) shows two electrical needle probes, connected to a semiconductor characterization system (Keithley 4200, Tektronix, Beaverton, OR, USA) placed into a sample 0.75 mm apart, with each needle in the same line of aligned NCCFs (Fig. 2(b)) to measure the electrical conductivity along a line of NCCFs, or one needle each in adjacent parallel lines of aligned NCCFs (Fig. 2(c)) to measure the electrical conductivity between adjacent lines of aligned NCCFs. The conductivity was determined from the electrical current between the two probes throughout a −20 to 20 V voltage sweep and used to compute the electrical resistance between both probes. The electrical conductivity results were categorized into less than 50 Ohms (electrically conductive) or more than 50 Ohms (electrically insulating). Electrical conductivity was measured in 15 different locations along the parallel lines of NCCFs and 5 different locations between adjacent lines of aligned NCCFs, or in 15 different locations for a control sample.

2.5. Mechanical characterization

The (static) mechanical properties were quantified for five samples fabricated with 1 wt percent NCCFs at each of the three ultrasound frequencies, and five control samples, i.e., a total of 20 samples. In addition, five samples fabricated with each of the three ultrasound frequencies, and five control samples, at 3 and 5 wt percent NCCFs were also tested for an additional 40 samples. A tensile testing frame (Instron 5967 Universal Testing System, Instron, Norwood, MA, USA) in the tensile pull-apart mode with a cross-head speed of 10 mm/min was used. The dimensions of the cross-section and the length of each printed single-layer sample were measured prior to each test to allow for stress and strain quantification. Each sample was loaded until failure. Two elastic moduli (due to the biphasic stress-strain response of the photopolymer resin), the ultimate tensile stress, and the strain at failure were extracted from each tensile experiment and used to characterize the flexibility and malleability of the samples as a function of the ultrasound frequency used during fabrication. The elastic moduli were determined by computing the slope of the stress-

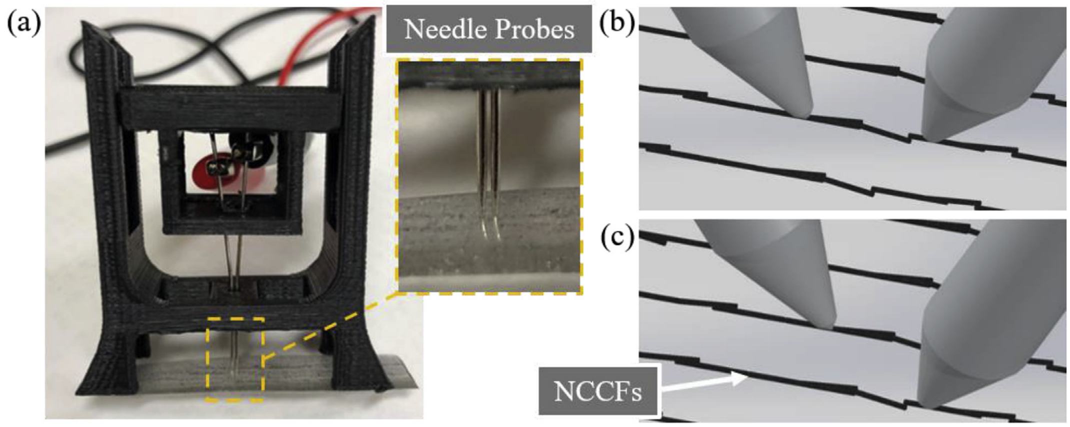

Fig. 2. (a) Custom fixture used to place needle probes during electrical conductivity measurements. (b) Diagram of a same line measurement for electrical conductivity. (c) Diagram of a neighboring line measurement for electrical conductivity.

strain response in the two unique phases of the response curve; the first starting at initial loading and going to an observable transition point and the second ranging from the transition point to failure of the sample.

2.6. Statistical analysis

The perpendicular distance between parallel lines of aligned NCCFs in each set of samples fabricated with each ultrasound frequency (0 Hz, 1.0 MHz, 1.5 MHz, and 2.0 MHz) and the pixel gray value spread for each ultrasound frequency and print speed combination were analyzed in the statistical computing environment R (The R Foundation, Vienna, Austria) via one-way analyses of variance (ANOVA) with a statistical power $\alpha = 0.05$. If the one-way ANOVA test resulted in significant differences between the calculated sample means, a Tukey's honest significant difference (HSD) test was performed for $\alpha = 0.05$, and provided a pairwise comparison between each sample set to determine which of the individual sets showed statistically significant differences.

The categorical results of each electrical conductivity test being either electrically conductive or electrically insulating were analyzed via a one-way ANOVA for $\alpha = 0.05$ to compare the number of electrically conductive measurements in sample groups between different ultrasound operating frequencies and print speeds. If the one-way ANOVA test resulted in significant differences between the calculated sample means, a Tukey's HSD test was performed for $\alpha = 0.05$ to determine which of the individual sets had statistically significant differences.

Each of the four mechanical properties measured during tensile testing were analyzed via a one-way ANOVA for $\alpha = 0.05$ to determine if there were any statistical differences between any of the mechanical properties with respect to the different operating frequencies, including the control. The mechanical properties were not expected to improve with the addition of linearly aligned features of micro-scale discontinuous NCCFs [38]. However, the mechanical properties were analyzed to study any changes in mechanical performance due to the evolution of samples from randomly dispersed networks of NCCFs to purposefully formed hierarchical structures of linearly aligned features of NCCFs with varying spacing.

3. Results and discussion

Fig. 3(a) shows four typical, single-layer samples, fabricated with different ultrasound frequencies and, thus, a different number of discontinuous aligned NCCF lines throughout each sample. Fig. 3(b) and (c) show magnified views of a control sample and a sample printed with an ultrasound operating frequency of 1.0 MHz and a print speed of 2.15 mm/s, respectively. The control sample has randomly dispersed NCCFs throughout the entire cross section whereas the sample exposed to the ultrasound field shows linear features of aligned NCCFs (emphasized with red lines). Fig. 3(d) shows an SEM image of a fractured cross section of a sample and, in the expanded image shows a single line of concentrated NCCFs with areas without NCCFs on either side.

Fig. 4 shows the orthogonal distance between parallel lines of aligned NCCFs as a function of the ultrasound DW operating frequency. The results are shown using the mean value ± one standard deviation where $n = 720$ for each sample group. The ANOVA showed at least one sample mean that was statistically significant from the other datasets with different ultrasound operating frequency for $\alpha = 0.05$ ($p < 10^{-6}$). A Tukey's HSD test was then used to show that statistically significant differences existed for the orthogonal distance measurement between lines of aligned NCCFs for all pairwise combinations of the three different ultrasound operating frequencies ($p < 10^{-6}$), indicated by unique Greek letters on the figure for each sample group that showed statistically significant differences.

Qualitatively, the clarity and consistency of the lines of aligned NCCFs varied between different individual samples and sample sets fabricated at constant ultrasound operating frequencies. However, optically magnified (see insets of Fig. 4) the lines of aligned NCCFs were identified by means of the relative fiber density, showing a higher relative fiber density within than between lines of aligned NCCFs. These distinct areas corresponded to the nodes (high relative fiber density) and anti-nodes (low relative fiber density) of the standing pressure wave established in the custom nozzle by the ultrasound transducer. Because the compressibility of the NCCFs is higher than that of the surrounding photopolymer resin, the acoustic radiation force associated with the standing pressure wave drives the NCCFs away from the anti-nodes towards the nodes of the standing pressure wave, where the acoustic radiation force vanishes [27].

Fig. 5 shows a typical result of the average pixel gray value for a sample fabricated with an ultrasound operating frequency of 1.0 MHz, a print speed of 2.15 mm/s, and 1 wt percent NCCFs, as a function of the distance across the width of the sample. The maximum and minimum average pixel gray values coincide with the lines of aligned NCCFs and the space between them, respectively.

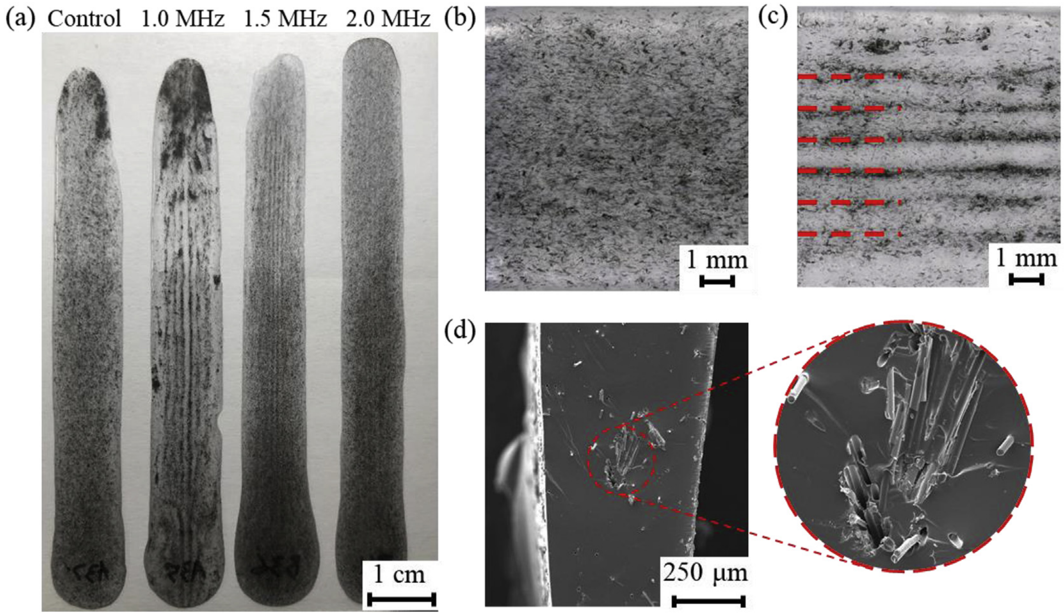

Fig. 3. (a) Examples of the samples made with the ultrasound DW process. (b) Image of a printed control sample with randomly dispersed NCCFs throughout. (c) Image of a printed sample with linearly aligned NCCFs. (d) SEM image of a sample cross section showing a linear feature concentration of NCCFs (in the expanded image).

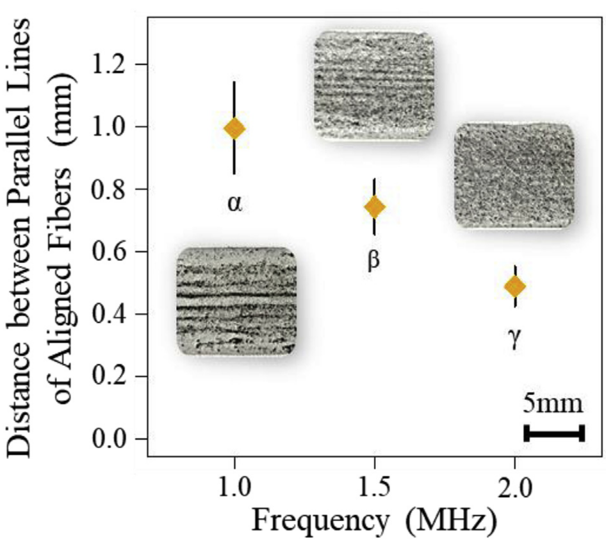

Fig. 4. Distance between parallel lines of aligned fibers plotted with respect to the sample operating frequency with images of samples printed at the indicated operating frequency.

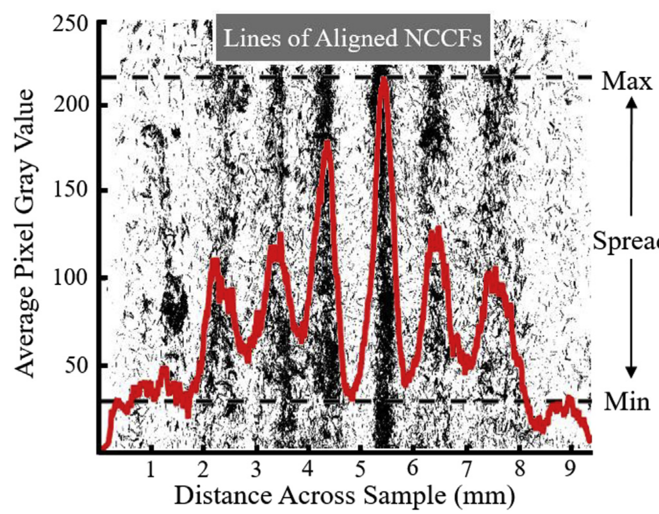

Fig. 5. Thresholded image of a printed sample overlaid with a plot of the average pixel gray value as a function of the distance across the sample width.

Fig. 6(a) shows optical microscope images of typical samples fabricated using the ultrasound DW process, with three different print speeds and ultrasound operating frequencies. Lines of aligned NCCFs were observed for all combinations of ultrasound operating frequency and print speed; however, the clarity of these lines decreased with increasing print speed, which was quantified by the spread value of the average pixel gray value. Fig. 6(b) shows the spread of average pixel gray values as a function of the print speed, for the three different operating frequencies. The results are represented with the mean value ± one standard deviation with $n = 6$ for each sample group. ANOVA analyses showed statistically significant differences of the average pixel gray value with respect to the print speed (for 1.0 MHz: $p < 10^{-3}$, for 1.5 MHz: $p < 10^{-6}$, for 2.0 MHz: $p < 10^{-5}$). A subsequent Tukey's HSD test then identified statistically significant differences between the average pixel gray value spread and each of the three print speeds for each ultrasound operating frequency (maximum p-values between each pair-wise comparison for 1.0 MHz: $p < 0.0372$, for 1.5 MHz: $p < 0.0002$, and for 2.0 MHz: $p < 0.0219$), indicated by unique Greek letters on the figure for each sample group that showed statistically significant differences and matching Greek letters for each sample group that did not show statistically significant differences. The results showed the average pixel gray spread value decreased with increased print speed, indicating that the difference between the relative fiber density of the lines of aligned NCCFs and the neighboring areas decreased, which affected the clear demarcation of the parallel lines of aligned NCCFs. Increased print speed requires increased flow rate of the photopolymer resin/NCCF mixture through the custom nozzle and, thus, the amount of ultrasound energy (given a constant ultrasound intensity for all experiments in this work) absorbed by the mixture decreased, which affected the quality of the NCCF alignment. Increasing the intensity of the

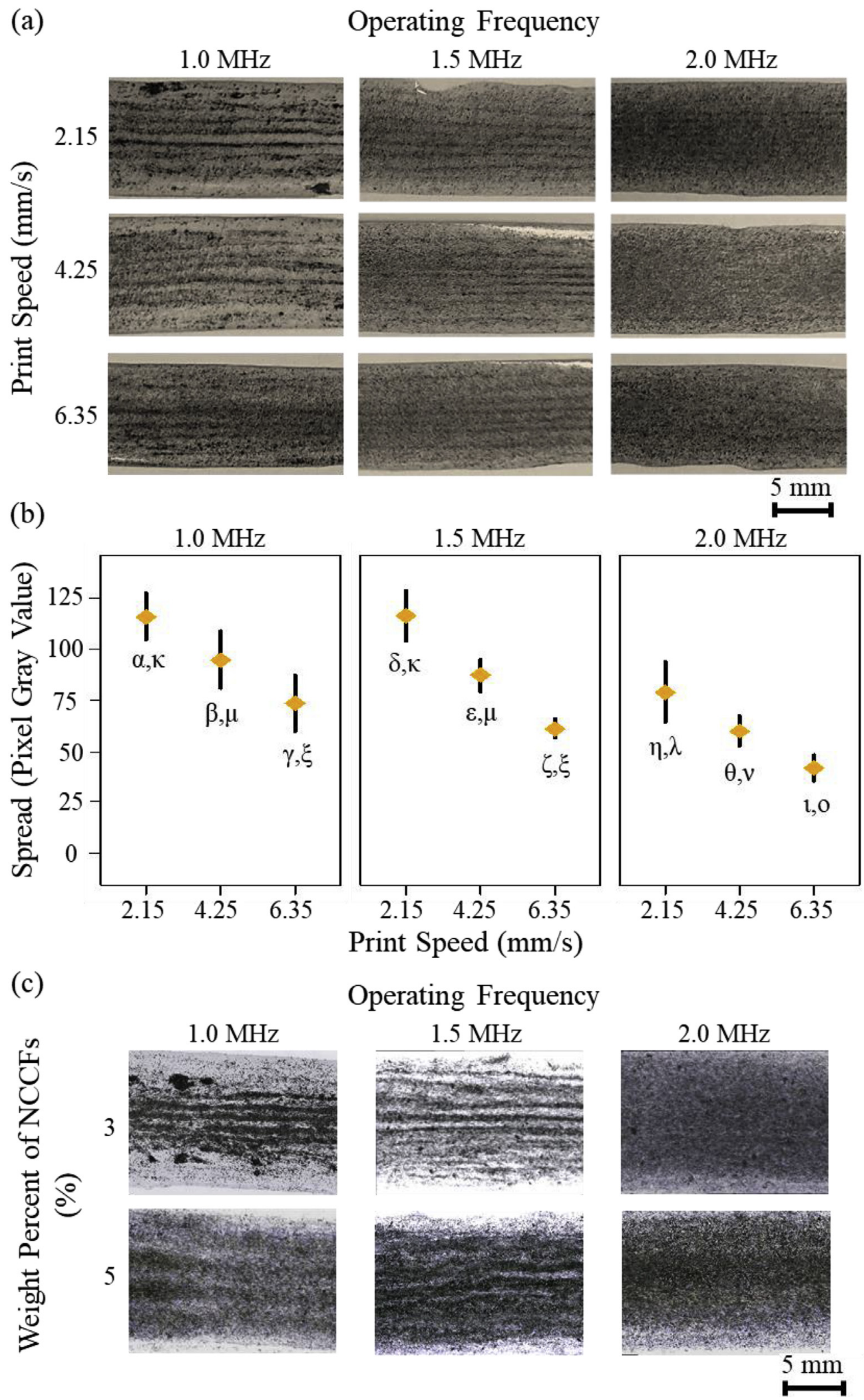

Fig. 6. (a) Images of samples at the specified operating frequency and print speed. (b) Measured spread value plotted with respect to the print speed and operating frequency. (c) Images of samples printed with higher weight percent of NCCFs.

ultrasound wave field (e.g., increasing the amplitude of the standing pressure wave) when increasing the print speed counteracts this phenomenon. However, increasing ultrasound intensity is limited by thermal heating and acoustic streaming within the custom nozzle [39–41].

Fig. 6(c) shows samples printed with 3 and 5 wt percent NCCFs and illustrates the difficulty in aligning fibers when using more than 1 wt percent NCCFs. Previous work has described the effects of increased particle loading rates in conjunction with ultrasound directed self-assembly [42]. Of note, the tensile properties of these materials were tested, but did not show an increase in the ultimate stress (with mean ± one standard deviation values of 6.22 MPa ±0.32 MPa, 5.91 MPa ±1.0 MPa, and 4.4 MPa ±0.55 MPa, for 1, 3, and 5 wt percent, respectively) when compared to samples with 1 wt percent NCCFs. As no increase in the strength was observed and the line features were more difficult to observe in most cases, they were not tested for electrical conductivity.

Fig. 7(a) shows the electrical current versus voltage for typical electrical conductivity measurements of two samples; one sample fabricated with an electrically conductive result (orange solid line) and a control sample showing an electrically insulating result (red dashed line). The electrical resistance was quantified in the linear region (Ohm's law) of the measurement. The electrical conductivity tests showed that samples with linear features of NCCFs possessed enhanced conductivity along those linear features for the distance used in the testing (0.75 mm). The average resistance for the electrically conductive measurements along lines of aligned NCCFs was 6.69 Ω with a standard deviation of ±2.07 Ω. The average resistance for the electrically insulating measurements along lines and between neighboring lines of aligned NCCFs was 1.89×10^{11} Ω with a standard deviation of $\pm 2.03 \times 10^{11}$ Ω. Summing all measurements, the electrical conductivity measurements showed 0 conductive and 45 insulating measurements in the control samples, 0 conductive and 90 insulating measurements between neighboring lines of aligned NCCFs (within the same sample), and 73 conductive and 197 insulating measurements along lines of aligned NCCFs. Hence, these results showed that electrical conductivity resulted from the alignment of the NCCFs within the photopolymer resin, forming a percolated network of fibers.

To further investigate why only some of the electrical conductivity measurements along lines of aligned NCCFs revealed an electrical conductive path, a sample was observed with optical microscopy during the needle probe placement and subsequent measurement. As expected, electrical conductivity was measured only when adjacent fibers were observed to be in end-to-end contact, providing a continuous path connecting the two needle probes. End-to-end contact of fibers occurred almost exclusively in lines of aligned NCCFs, but was not continuous throughout the length of each sample. Continuous sections of end-to-end contact of NCCFs were observed as short as 0.3 mm and up to 4.8 mm in length. Short breaks in continuity on the order of 50–500 μm between adjacent fibers were observed in each sample, regardless of ultrasound operating frequency and print speed. The relationship between these short breaks and the electrical conductivity of each sample was analyzed as the fraction of electrically conductive measurements resulting from all measurements as a function of ultrasound operating frequency and print speed. Fig. 7(b) shows the fraction of electrically conductive measurements as a function of the ultrasound operating frequency and print speed, respectively, with the data represented as the mean ± one standard deviation. Note that results are shown for the control in only the frequency graph, as no conductive measurements were recorded in any control. ANOVA analyses showed a statistically significant difference in the average number of electrically conductive measurements in samples between different ultrasound operating frequencies ($p < 10^{-5}$). However, no statistically significant differences existed between the average number of electrically conductive measurements in samples between different print speeds ($p = 0.5890$), indicated by matching Greek letters on the figure for each sample group with no statistically significant differences. A post-hoc Tukey HSD test showed that there were statistically significant differences between each operating frequency and the control ($p < 0.002$ for each pairwise comparison) as well as between the 1.0 MHz and 2.0 MHz samples ($p = 0.0078$), indicated by unique Greek letters on the figure for each sample group that showed statistically significant differences.

Table 1 summarizes the result of the mechanical tensile testing of the samples fabricated using ultrasound DW. Each row shows the mean of the five samples fabricated at each ultrasound operating frequency and the control samples, in addition to the mean and standard deviation for all tested samples and the p-value from the ANOVA test for each mechanical property. Fig. 8 shows typical examples of the stress-strain curves resulting from the tensile testing of a control sample (red solid line) and samples fabricated at each ultrasound operating frequency (1.0 MHz: green dashed line, 1.5 MHz: orange dotted line, 2.0 MHz: black dot-dash line). The results showed minimal differences between samples fabricated at different ultrasound operating frequencies with regards to any of the four mechanical properties presented. The p-values of each ANOVA test confirmed that no statistically significant differences existed between any sample sets for any of the mechanical properties measured. These results indicated that aligning the NCCFs in

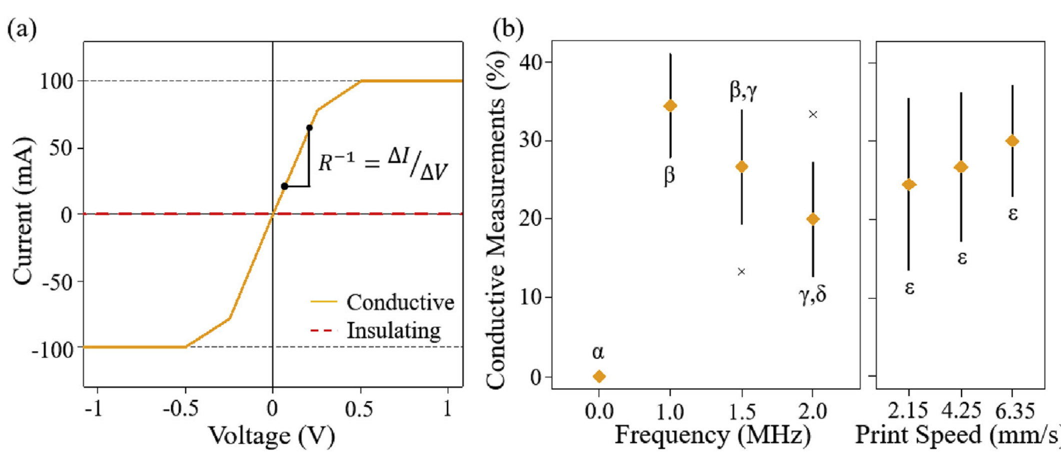

Fig. 7. (a) Two typical conductivity test results (conductive or insulating). (b) Percentage of conductive test as a function of operating frequency and print speed.

Table 1
Data from mechanical testing where each value is the mean of n = 5 measurements. The mean and standard deviation (SD) columns were calculated for each mechanical property across all sample results. The p-value column shows the calculated p-value from the one-way ANOVA analysis conducted on each mechanical property with respect to the operating frequencies and control samples.

	Control	1.0 MHz	1.5 MHz	2.0 MHz	Mean	SD	p-value
1st Modulus [MPa]	171	191	137	158	164	23.0	0.34
2nd Modulus [MPa]	16.3	16.5	16.6	14.8	16.0	0.86	0.67
Ultimate Stress [MPa]	6.66	6.15	6.06	5.88	6.22	0.32	0.52
Strain at Failure [%]	0.27	0.22	0.26	0.25	0.25	0.02	0.26

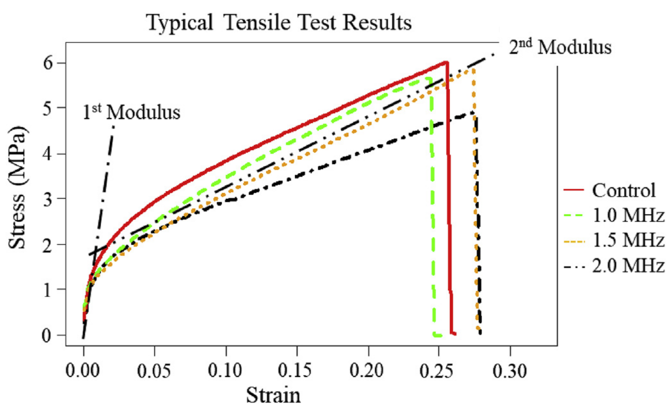

Fig. 8. Example tensile test results for samples loaded until failure. The results are for samples with 1 wt percent CNNFs.

a sample did not affect the macroscopic mechanical performance of the sample, for the weight percent dispersed in the photopolymer resin in this work. Comparing the mean value of both moduli of the samples (164 MPa and 16.0 MPa) with those of other commonly used electrical conductors showed that the ultrasound DW samples displayed lower moduli than copper (210 GPa [43]) or gold (77 GPa [44]), noting the limitations (discussed previously) of the ultrasound DW specimens as electrical conductors. As such, the ultrasound DW samples were much more flexible and malleable than commonly used electrical conductors.

Previous research into 3D printing engineered materials with polymer matrix composites has focused on achieving results that demonstrate more useful structural or functional characteristics that were not attainable by any of the constituent materials by themselves, with a primary focus on enhancing material properties such as tensile strength and electrical conductivity while still being able to control the complex internal structures and organization of the engineered materials [45]. The ultrasound DW method presented in this work demonstrates control over the alignment of fibers in a photopolymer matrix material, which expands the possible particle/fiber placement because of the process's ability to create part geometries without the need of a mold or container. Though 3D printed carbon fiber reinforced composites have been shown to have increased tensile strength and Young's modulus [7,46,47], the samples produced and tested in this research have managed to integrate internal structuring of NCCFs while maintaining flexible characteristics. Additionally, similar to results in other research using conductive additives in polymer matrix composites [31,47,48], the samples from this research have been shown to possess areas of electrical conductivity by orienting high-aspect ratio fibers in an end-to-end contact fashion and creating lines of aligned fibers, essentially creating individual conductor paths through each sample. These lines of aligned fibers mimic natural matrix materials with fibrous linear alignment seen in nature, such as those found in the composite structure of a dactyl club of mantis shrimp [3]. The unique structures and material properties observed in the samples produced by this new manufacturing process could lead to applications in integrated conductor assemblies including flexible electronics, such as one-off flexible biosensors and electrodes tailored to individual patients, application area, or conductor sensor requirements, integration of electrical conductors through dynamic mechanical joints, or other energy applications such as electromagnetic shielding or cloaking of 3D printed assemblies or thermal dissipation and sinking.

4. Conclusions

This work demonstrated a manufacturing process that produces flexible engineered materials containing user-defined micro-substructures through the combination of direct-write 3D printing and ultrasound directed self-assembly. The following conclusions were made:

- Using an ultrasound field to apply extrinsic control over the alignment of NCCFs dispersed in a liquid medium during the 3D DW printing process enabled manufacturing single-layer materials with aligned NCCFs.
- The number of parallel lines of aligned NCCFs in a sample (6, 10, and 13 visible lines for 1.0 MHz, 1.5 MHz, and 2.0 MHz, respectively) is determined by varying the ultrasound operating frequency.
- Statistically significant differences existed between the orthogonal distance between lines of aligned NCCFs and each of the ultrasound operating frequencies. Changing the printing speed did not cause any statistically significant differences in the orthogonal distance between lines of aligned NCCFs.
- Statistically significant fractions of all electrical conductivity measurements across samples printed with ultrasound as opposed to the control samples existed. Additionally, statistically significant fractions of all electrical conductivity measurements across samples with different operating frequencies (1.0 MHz and 2.0 MHz) also existed.
- No significant difference in any of the mechanical properties existed between samples with and without aligned NCCFs, including two separate moduli, ultimate tensile strength, and elongation at failure.
- The ultrasound DW technique created flexible single layer samples with integrated lines of aligned NCCFs inspired by biological and natural materials. Using electrically conductive fibers enabled sections of the engineered material to be electrically conductive and, therefore could potentially be used in shielding or other energy applications.

CRediT authorship contribution statement

Paul Wadsworth: Data curation, Formal analysis, Writing - original draft, Writing - review & editing. **Isaac Nelson:** Data curation, Formal analysis, Writing - original draft. **Debora Lyn

Porter: Data curation, Formal analysis. **Bart Raeymaekers:** Writing - original draft, Writing - review & editing, Funding acquisition. **Steven E. Naleway:** Project administration, Writing - original draft, Writing - review & editing, Funding acquisition.

Acknowledgements

This work was financially supported in part by the National Science Foundation under grant CMMI #1660979.

References

[1] S.E. Naleway, M.M. Porter, J. McKittrick, M.A. Meyers, Structural design elements in biological materials: application to bioinspiration, Adv. Mater. 27 (37) (2015) 5455–5476, https://doi.org/10.1002/adma.201502403.
[2] A.R. Studart, Towards high-performance bioinspired composites, Adv. Mater. 24 (37) (2012) 5024–5044, https://doi.org/10.1002/adma.201201471.
[3] J.C. Weaver, G.W. Milliron, K. Evans-Lutterodt, S. Herrera, I. Gallana, W.J. Mershon, B. Swanson, P. Zavattieri, E. DiMasi, D. Kisailus, The stomatopod dactyl club: a formidable damage-tolerant biological hammer, Science 336 (6086) (2012) 1275–1280, https://doi.org/10.1126/science.1218764.
[4] E.A. Zimmermann, B. Gludovatz, E. Schaible, N.K.N. Dave, W. Yang, M.A. Meyers, R.O. Ritchie, Mechanical adaptability of the bouligand-type structure in natural dermal armour, Nat. Commun. 4 (2634) (2013), https://doi.org/10.1038/ncomms3634.
[5] E. Munch, M.E. Launey, D.H. Alsem, E. Saiz, A.P. Tomsia, R.O. Ritchie, Tough, bio-inspired hybrid materials, Science 322 (5907) (2008) 1516–1520, https://doi.org/10.1126/science.1164865.
[6] M.M. Porter, J. Mckittrick, M.A. Meyers, Biomimetic materials by freeze casting, JOM (J. Occup. Med.) 65 (6) (2013) 720–727, https://doi.org/10.1007/s11837-013-0606-3.
[7] F. Ning, W. Cong, J. Qiu, J. Wei, S. Wang, Additive manufacturing of carbon fiber reinforced thermoplastic composites using fused deposition modeling, Compos. B Eng. 80 (2015) 369–378, https://doi.org/10.1016/j.compositesb.2015.06.013.
[8] T.A. Ogden, M. Prisbrey, I. Nelson, B. Raeymaekers, S.E. Naleway, Ultrasound freeze casting: fabricating bioinspired porous scaffolds through combining freeze casting and ultrasound directed self-assembly, Mater. Des. 164 (2019), 107561, https://doi.org/10.1016/j.matdes.2018.107561.
[9] L. Kong, W. Chen, Carbon nanotube and graphene-based bioinspired electrochemical actuators, Adv. Mater. 26 (7) (2014) 1025–1043, https://doi.org/10.1002/adma.201303432.
[10] W. Zhang, Y. Zhou, K. Feng, J. Trinidad, A. Yu, B. Zhao, Morphologically controlled bioinspired dopamine-polypyrrole nanostructures with tunable electrical properties, Adv. Electron. Mater. 1 (11) (2015), 1500205, https://doi.org/10.1002/aelm.201500205.
[11] Y.-Q. Li, T. Yu, T.-Y. Yang, L.-X. Zheng, K. Liao, Bio-inspired nacre-like composite films based on graphene with superior mechanical, electrical, and biocompatible properties, Adv. Mater. 24 (25) (2012) 3426–3431, https://doi.org/10.1002/adma.201200452.
[12] M.R. Begley, D.S. Gianola, T.R. Ray, Bridging functional nanocomposites to robust macroscale devices, Science 364 (6447) (2019), https://doi.org/10.1126/science.aav4299 eaav4299.
[13] J.J. Martin, B.E. Fiore, R.M. Erb, Designing bioinspired composite reinforcement architectures via 3D magnetic printing, Nat. Commun. 6 (2015) 8641, https://doi.org/10.1038/ncomms9641.
[14] R.M. Erb, K.H. Cherenack, R.E. Stahel, R. Libanori, T. Kinkeldei, N. Munzenrieder, G. Troster, A.R. Studart, Locally reinforced polymer-based composites for elastic electronics, Appl. Mater. Interfaces 4 (6) (2012) 2860–2864, https://doi.org/10.1021/am300508e.
[15] R.M. Erb, R. Libanori, N. Rothfuchs, A.R. Studart, Composites reinforced in three dimensions by using low magnetic fields, Science 335 (6065) (2012) 199–204, https://doi.org/10.1126/science.1210822.
[16] I. Nelson, S.E. Naleway, Intrinsic and extrinsic control of freeze casting, J. Mater. Res. Technol. 8 (2) (2019) 2372–2385, https://doi.org/10.1016/j.jmrt.2018.11.011.
[17] I. Nelson, T.A. Ogden, S.A. Khateeb, J. Graser, T.D. Sparks, J.J. Abbott, S.E. Naleway, Freeze-casting of surface-magnetized iron(II,III) oxide particles in a uniform static magnetic field generated by a helmholtz coil, Adv. Eng. Mater. 21 (3) (2019), 1801092, https://doi.org/10.1002/adem.201801092.
[18] I. Nelson, L. Gardner, K. Carlson, S.E. Naleway, Freeze casting of iron oxide subject to a tri-axial nested helmholtz-coils driven uniform magnetic field for tailored porous scaffolds, Acta Mater. 173 (2019) 106–116, https://doi.org/10.1016/j.actamat.2019.05.003.
[19] K.D. Hermanson, S.O. Lumsdon, J.P. Williams, E.W. Kaler, O.D. Velev, Dielectrophoretic assembly of electrically functional microwires from nanoparticle suspensions, Science 294 (5544) (2001) 1082–1086, https://doi.org/10.1126/science.1063821.
[20] Y. Yang, Z. Chen, X. Song, Z. Zhang, J. Zhang, K.K. Shung, Q. Zhou, Y. Chen, Biomimetic anisotropic reinforcement architectures by electrically assisted nanocomposite 3D printing, Adv. Mater. 29 (11) (2017), 1605750, https://doi.org/10.1002/adma.201605750.
[21] P. Huang, Z. Xia, S. Cui, 3D printing of carbon fiber-filled conductive silicon rubber, Mater. Des. 142 (2018) 11–21, https://doi.org/10.1016/j.matdes.2017.12.051.
[22] Z. Fan, J.C. Ho, T. Takahashi, R. Yerushalmi, K. Takei, A.C. Ford, Y.L. Chueh, A. Javey, Toward the development of printable nanowire electronics and sensors, Adv. Mater. 21 (2009) 3703–3743, https://doi.org/10.1002/adma.200900860.
[23] H.N. Chia, B.M. Wu, Recent advances in 3D printing of biomaterials, J. Biol. Eng. 9 (4) (2015), https://doi.org/10.1186/s13036-015-0001-4.
[24] A.R. Studart, Additive manufacturing of biologically-inspired materials, Chem. Soc. Rev. 45 (2) (2016) 359–376, https://doi.org/10.1039/C5CS00836K.
[25] P.V. Kamat, K.G. Thomas, S. Barazzouk, G. Girishkumar, K. Vinodgopal, D. Meisel, Self-assembled linear bundles of single wall carbon nanotubes and their alignment and deposition as a film in a dc field, J. Am. Chem. Soc. 126 (34) (2004) 10757–10762, https://doi.org/10.1021/ja0479888.
[26] M. Fujiwara, E. Oki, M. Hamada, Y. Tanimoto, I. Mukouda, Y. Shimomura, Magnetic orientation and magnetic properties of a single carbon nanotube, J. Phys. Chem. A 105 (18) (2001) 4383–4386, https://doi.org/10.1021/jp004620y.
[27] B. Raeymaekers, C. Pantea, D.N. Sinha, Manipulation of diamond nanoparticles using bulk acoustic waves, J. Appl. Phys. 109 (2011), 014317, https://doi.org/10.1063/1.3530670.
[28] R.R. Collino, T.R. Ray, R.C. Fleming, J.D. Cornell, B.G. Compton, M.R. Begley, Deposition of ordered two-phase materials using microfluidic print nozzles with acoustic focusing, Extrem. Mech. Lett. 8 (2016) 96–106, https://doi.org/10.1016/j.eml.2016.04.003.
[29] J. Greenhall, F.G. Vasquez, B. Raeymaekers, Ultrasound directed self-assembly of user-specified patterns of nanoparticles dispersed in a fluid medium, Appl. Phys. Lett. 108 (2016), 103103, https://doi.org/10.1063/1.4943634.
[30] M. Prisbrey, J. Greenhall, F.G. Vasquez, B. Raeymaekers, Ultrasound directed self-assembly of three-dimensional user-specified patterns of particles in a fluid medium, J. Appl. Phys. 121 (2017), 014302, https://doi.org/10.1063/1.4973190.
[31] T.M. Llewellyn-Jones, B.W. Drinkwater, R.S. Trask, 3D printing components with ultrasonically arranged microscale structure, Smart Mater. Struct. 25 (2) (2016), 02LT01, https://doi.org/10.1088/0964-1726/25/2/02LT01.
[32] J. Greenhall, B. Raeymaekers, 3D printing macroscale engineered materials using ultrasound directed self-assembly and stereolithography, Adv. Mater. Technol. 2 (9) (2017), 1700122, https://doi.org/10.1002/admt.201700122.
[33] M.D. Haslam, B. Raeymaekers, Aligning carbon nanotubes using bulk acoustic waves to reinforce polymer composites, Composites Part B 60 (2014) 91–97, https://doi.org/10.1016/j.compositesb.2013.12.027.
[34] D. Haydock, Calculation of the radiation force on a cylinder in a standing wave acoustic field, J. Phys. A Math. Gen. 38 (2005) 3279–3285, https://doi.org/10.1088/0305-4470/38/15/004.
[35] F.G. Mitri, Theoretical calculation of the acoustic radiation force acting on elastic and viscoelastic cylinders placed in a plane standing or quasistanding wave field, Eur. Phys. J. B 44 (1) (2005) 71–78, https://doi.org/10.1140/epjb/e2005-00101-0.
[36] W. Wei, D.B. Thiessen, P.L. Marston, Acoustic radiation force on a compressible cylinder in a standing wave, J. Acoust. Soc. Am. 116 (1) (2004) 201, https://doi.org/10.1121/1.1753291.
[37] J. Wu, G. Du, S.S. Work, D.M. Warshaw, Acoustic radiation pressure on a rigid cylinder: an analytical theory and experiments, J. Acoust. Soc. Am. 87 (2) (1990) 581–586, https://doi.org/10.1121/1.398927.
[38] W.D. Callister Jr., D.G. Rethwisch, Materials Science and Engineering: an Introduction, Wiley, Hoboken, NJ, 2014.
[39] A.L. Bernassau, P. Glynne-Jones, F. Gesellchen, M. Riehle, M. Hill, D.R. Cumming, Controlling acoustic streaming in an ultrasonic heptagonal tweezers with application to cell manipulation, Ultrasonics 54 (1) (2014) 268–274, https://doi.org/10.1016/j.ultras.2013.04.019.
[40] M. Wiklund, R. Green, M. Ohlin, Applications of acoustic streaming in microfluidic devices, Lab Chip 12 (2012) 2438–2451, https://doi.org/10.1039/C2LC40203C.
[41] P. Ronkanen, P. Kallio, M. Vilkko, H.N. Koivo, Self heating of piezoelectric actuators measurement and compensation, Proceeding of the IEEE, in: International Symposium on Micro-nanomechatronics and Human Science; Nagoya, Japan, 2004, pp. 313–318.
[42] J. Greenhall, L. Homel, B. Raeymaekers, Ultrasound directed self-assembly processing of nanocomposite materials with ultra-high carbon nanotube weight fraction, J. Compos. Mater. 53 (10) (2019) 1329–1336, https://doi.org/10.1177/0021998318801452.
[43] N. Alok, The Metals Databook, McGraw-Hill, New York, 1997.
[44] H.E. Boyer, et al., Metals Handbook, American Society for Metals, Metals Park, Ohio, 1984.
[45] X. Wang, M. Jiang, Z. Zhou, J. Gou, D. Hui, 3D printing of polymer matrix composites: a review and prospective, Compos. B Eng. 110 (2017) 442–458, https://doi.org/10.1016/j.compositesb.2016.11.034.
[46] H.L. Tekinalp, V. Kunc, G.M. Velez-Garcia, C.E. Duty, L.J. Love, A.K. Naskar, C.A. Blue, S. Ozcan, Highly oriented carbon fiber-polymer composites via additive manufacturing, Compos. Sci. Technol. 105 (2014) 144–150, https://doi.org/10.1016/j.compscitech.2014.10.009.
[47] L.J. Love, V. Kunc, O. Rios, C.E. Duty, A.M. Elliott, B.K. Post, R.J. Smith, C.A. Blue, The importance of carbon fiber to polymer additive manufacturing, J. Mater. Res. 29 (17) (2014) 1893–1898, https://doi.org/10.1557/jmr.2014.212.
[48] B.G. Compton, J.A. Lewis, 3D-printing of lightweight cellular composites, Adv. Mater. 26 (34) (2014) 5930–5935, https://doi.org/10.1002/adma.201401804.